Zeitschrift für **METALLKUNDE**

International Journal
of Materials Research and
Advanced Techniques

A Applied

Paul H. Mayrhofer, Helmut Clemens, Christian Mitterer
Department of Physical Metallurgy and Materials Testing, University of Leoben, Leoben, Austria

Interfaces in nanostructured thin films and their influence on hardness

Nanocrystalline structures have attracted increasing interest in modern development of hard films for wear-resistant applications. In plasma-assisted vapor-deposited thin films, nanostructures can be generated during growth or post-annealing treatment. In this review, we demonstrate, using the four model-films overstoichiometric TiB_2, $TiN-TiB_2$, Ti(B)N, and $Ti_{0.33}Al_{0.67}N$, how interfaces influence the mechanical properties of ceramic thin films. For overstoichiometric TiB_2 films and $TiN-TiB_2$, a two-dimensional and three-dimensional nanostructure, respectively, is generated during growth by segregation-driven processes. Growth of less B containing Ti(B)N films and $Ti_{0.33}Al_{0.67}N$ results in the formation of a supersaturated TiN phase with NaCl structure, where either the non-metallic part or the metallic part is substituted by B or Al, respectively. For these films, the nanostructure forms during post-annealing, due to the decomposition of the supersaturated phases into their stable constituents. As the hardness of a material is determined by resistance to bond distortion and, dislocation formation and motion, which themselves depend on the amount of interfaces and their constitution, there is a direct relation between hardness and nanostructure.

Keywords: Interfaces, Nanocomposite; Supersaturation; Age Hardening; Thin Films

1. Introduction

Nanostructured thin films of transition metal nitrides, carbides and borides are the topic of many papers due to their physical, chemical and mechanical properties which make them applicable for several industrial fields [1–38]. Basically, nanocrystalline materials are single- or multi-phased polycrystals with a typical crystal size of a few nanometers (1–100 nm) in at least one direction. Thus, they can be equiaxed or columnar in nature (three- or two-dimensional nanostructure, respectively), or they can consist of a layered nanostructure (one-dimensional nanostructure) [39].

The increasing industrial demand for advanced protective thin films with tailored properties requires the development of multi-elemental and/or multi-phase ceramic layers [40–59]. Hard films with increased amount of interfaces can reveal several interesting properties, such as high hardness and toughness, if their nanocrystalline arrangement is optimized. Increased hardness and toughness with decreasing grain size d is a well-known phenomenon and described by the Hall–Petch effect [60, 61]. The decreasing dislocation activity with decreasing grain size causes the hardness to increase [62]. For ductile materials, the yield strength can be estimated with the Tabor-relation [63] that hardness H (obtained from a Vickers indentation) is about three times of the yield strength [64]. For hard materials (like the thin films reported here) the hardness is better described by the Marsh-relation [65], which takes into account the elastic modulus E, the Poisson ratio ν, and the yield strength. Considering, that the theoretical strength of a solid is solely a function of the strength of the interatomic bonds which bind the atoms together, the theoretical maximum yield strength would be $E/10$ [66]. Thus, the theoretical hardness (obtained via a Vickers indentation and using the Marsh-relation) e. g., for TiN (E = 300–400 GPa, ν = 0.25) would be 40–53 GPa and for TiB_2 (E = 400–500 GPa, ν = 0.25) 53–66 GPa, respectively. In practice, however, the strength of inherently strong solids never meets these theoretical

expectations because of the presence of crystal imperfections, microscopic defects and cracks. This is also valid for materials composed of 1–2 nm sized crystals, which are considered to be dislocation-free [62].

If the grain size is smaller than a critical one (d_c), the increased volume fraction of interfaces (i. e., grain and phase boundaries, low-angle grain boundaries, …), with their typically lower resistance against deformation than dislocation-poor crystals, cause that the Hall–Petch effect ceases or even reverses [67–69]. Thus, especially for nanomaterials with $d \leq 5$ nm, the cohesive strength of the interfaces determines the strength of nanomaterials to a large extent [41–59, 70, 71]. Thin films, prepared by physical vapor deposition (PVD) or plasma-assisted chemical vapor deposition (PACVD), are known to have an increased hardness compared to their corresponding bulk counterparts, due to the deposition process and the high density of growth-defects [1–38, 72]. This hardening effect (which will be simply called growth-defect hardening) diminishes when the films are exposed to temperatures above the growth temperature, as recovery and recrystallization processes occur [17–38, 73].

Vepřek et al. [18–23] and Patscheider et al. [24] report that high hardness in nanocomposite thin films is obtained when small crystallites are separated by a thin (1–2 monolayer, ML) boundary phase with high cohesive strength. They deposited films within the system $TiN-Si_3N_4$ where nanocrystals of TiN, due to a segregation-driven renucleation, are embedded in an amorphous matrix. Vepřek and co-workers [19, 23] showed also, that hardness which is mainly the result of nanostructure (and hence of an increased amount of interfaces) can sustain higher annealing temperatures than hardness which is the result of growth-defect hardening. For advanced machining processes, like high-speed or dry cutting, the frictional heating during wear can cause temperatures in excess of 900 °C at the tool-workpiece contact areas. Therefore, the annealing behaviour of thin films used for such applications is of vital importance.

In this review, we demonstrate the formation of a two-dimensional and a three-dimensional nanostructure during growth of $TiB_{2.4}$ and $TiN-TiB_2$ layers, respectively. During post-annealing at temperatures (T_a) exceeding the growth temperature, where growth-defect hardening diminishes, the hardness for $TiB_{2.4}$ remains at ~ 60 GPa as its columnar nanostructure is unaffected by the heat treatment. This is in contrast to 30.5 at.% B containing $TiN-TiB_2$ thin films, which are composed of randomly oriented 2–3 nm sized TiN and TiB_2 crystals in the as-deposited state, where post-annealing gives rise to compact internal boundaries (interfaces) [74] and increases the crystallite sizes to ~ 5 nm. Consequently, the hardness increases from ~ 42 GPa to ~ 53 GPa during annealing at $T_a \leq 900$ °C. Further annealing at $T_a \geq 1000$ °C results in recrystallization processes, and hence the hardness decreases.

Growth of a 17.4 at.% B containing Ti(B)N film results in a columnar, single-phased supersaturated TiN structure, where B substitutes N due to limited atomic assembly kinetics during the deposition process [75]. A supersaturated TiN phase, where the metallic part (Ti) is replaced by Al, results during growth of a $Ti_{0.33}Al_{0.67}N$ film. These supersaturated phases are, however, metastable and tend to decompose during post-annealing into their stable constituents via the formation of nm-sized domains due to their limited solubility [26–29, 38, 76, 77]. This precipitation strengthening [64] effectively compensates the diminishing solid-solution and growth-defect hardening, consequently resulting in hardness values of ~ 44 GPa for Ti(B)N and ~ 39 GPa for $Ti_{0.33}Al_{0.67}N$ after annealing at T_a = 900 °C.

The nanostructure (arising during growth or post-annealing) and hence the increased amount of interfaces, which influence the nucleation and motion of dislocations, is responsible for high film-hardness even after annealing at temperatures above the growth temperature.

2. Experimental

The deposition systems, growth conditions and characterization techniques for the $TiB_{2.4}$, $TiN-TiB_2$, Ti(B)N, and $Ti_{0.33}Al_{0.67}N$ films used for this review are described in more detail in Refs. [78–80], and [17], respectively. For the sputtered films $TiB_{2.4}$ and $TiN-TiB_2$, the incident metal flux J_{Ti} was estimated based upon measured deposition rate R values, film composition (see next paragraph), film thickness, and assuming bulk density. The ion flux J_{Ar+} and the ion energy E_{Ar+} bombarding the growing film are determined using Langmuir-probe measurements following the procedures described in Ref. [81]. Incident ion/metal flux ratio J_{Ar+}/J_{Ti} and E_{Ar+} during sputtering are used to determine the growth conditions. The growth temperature for these two films is 300 °C. The supersaturated Ti(B)N film is prepared at 510 °C by using a commercial Rübig PACVD P40/60 system [3], and the $Ti_{0.33}Al_{0.67}N$ film is deposited at 500 °C by utilizing a commercial arc evaporation system (Metaplas MR323) [37]. The $TiB_{2.4}$, $TiN-TiB_2$, and Ti(B)N films are characterized in the as-deposited state and after annealing at temperatures $T_a \leq 1100$ °C at pressures $\leq 10^{-3}$ Pa (7.5×10^{-6} Torr) for 60 or 30 min, respectively. Additional annealing treatments of the films, removed from their substrate to prevent interdiffusion, are conducted at 1400 °C in a flow of Ar at atmospheric pressure. The heating and cooling rates for all annealing treatments are above 100 K/min.

The $TiB_{2.4}$, $TiN-TiB_2$, and Ti(B)N film chemical composition is determined by wavelength dispersive electron-probe microanalysis (EPMA) using a MICROSPEC WDX-3PC analyzer. Quantification is obtained by means of TiN and TiB_2 film standards, calibrated using nuclear reaction analyses (NRA). Film hardness H is obtained by computer-controlled measurements using a Fischerscope H100C with 50 mN load for which the Vickers indentation depth is ≤ 10 % of the film thickness. The chemical composition of $Ti_{0.33}Al_{0.67}N$ is obtained by energy-dispersive X-ray (EDX) analysis and Rutherford backscattering spectroscopy (RBS). Their film hardness is obtained by nanoindentation in the as-deposited state and after annealing at $T_a \leq 1250$ °C in a flow of argon at atmospheric pressure for 120 min [37]. Structure and morphology of the films are studied by Bragg-Brentano X-ray diffraction (XRD, Siemens D 500) with Cu Kα radiation, and transmission electron microscopy (TEM, JEOL 2010 LaB6) and high-resolution TEM (HRTEM, JEOL 2010F), respectively.

Differential scanning calorimetry (DSC) of the films is performed in a Netzsch-STA 409 calorimeter. To avoid the influence of the substrate material on the measurements, the films are removed chemically from the polished low-alloyed steel substrates using 10 mol% nitric acid. Dynamical

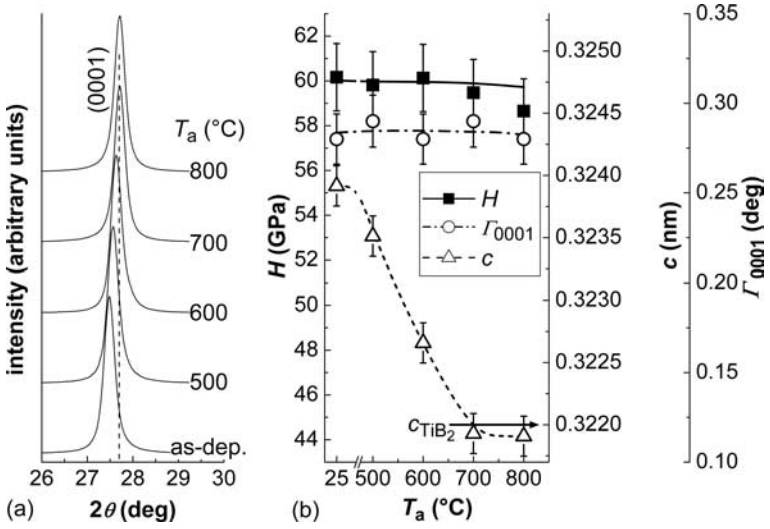

Fig. 1. (a) XRD patterns of an as-deposited $TiB_{2.4}$ film and samples which have been annealed for 1 h at temperatures T_a. (b) Hardness H, lattice constant c, and full-width-at-half-maximum intensity Γ of the (0001) XRD reflection as a function of T_a. For comparison, the lattice constant c of TiB_2 is indicated by an arrow.

DSC experiments, from room temperature up to 1400 °C at a heating rate of 50 K · min^{-1} are carried out in a flow of Ar (99.999 % purity and 50 sccm with atmospheric pressure) to protect the sample against oxidation, starting. Additionally, also these powdery samples are investigated by XRD after the DSC measurement up to 1400 °C.

3. Results on nanostructures

3.1. Nanostructures formed during growth

The simultaneous growth of immiscible phases by vapor deposition frequently leads to the formation of nanocrystalline materials. The amount and type of additional phases and elements can be used to control the orientation and the size of grains in the sputtered films [68]. The nanostructured materials may contain crystalline, quasicrystalline (i. e., hybrid of crystalline and amorphous), or amorphous phases and can consist of metals, ceramics or their composites. Here, we give an example for a two-dimensional nanostructure obtained in overstoichiometric TiB_2, where excess B is responsible for the formation of ~ 5 nm diameter TiB_2 nanocolumns. Furthermore, we show for TiN–TiB_2, that segregation-driven re-nucleation of 2–3 nm sized TiN and TiB_2 nanocrystals during growth results in the formation of a three-dimensional nanostructure.

3.1.1. Two-dimensional nanostructure of overstoichiometric TiB_2

TiB_2 crystallizes in the hexagonal C32 structure in which B is located in the interstices between (0001) close-packed Ti planes [82, 83]. Thus, B and Ti planes alternate along the c-axis [82, 83]. Reported lattice parameters are $a = 0.3038$ nm and $c = 0.3220$ nm [84, 85]. Primarily due to the strong covalent bonding in the B network, TiB_2 has a relatively narrow single-phase field with composition ranging from 65.6 to 66.7 at.% B, a high melting point (3225 °C), and a high hardness ($H = 25$ GPa) [83, 86, 87].

Recently, TiB_2 thin films deposited by *non-reactive* dc sputtering from compound targets have been shown to have much higher hardnesses, 48 to 77 GPa, which are not simply due to correspondingly high residual stresses and growth-defect hardening [4, 25]. The mechanism giving rise to this superhardness effect (defined in Refs. [23, 88] as $H \geq 40$ GPa) is based upon the nanocolumnar structure [78] of overstoichiometric TiB_2 layers with a pronounced (0001) texture [1, 7–10, 13, 25, 78, 82].

The only XRD peaks obtained from as-deposited and annealed $TiB_{2.4}$ layers grown on steel substrates over the 2θ range 20°–90° are the (0001) at 27.54° (see Fig. 1a) and the (0002) at 56.94°. The (0001) peak position continuously shifts from 27.54° (lattice constant $c = 0.3239$ nm) in the as-deposited state to 27.71° ($c = 0.3219$ nm) after annealing at 800 °C, as indicated in Figs. 1a and b. The lattice constant in the [0001] direction for bulk TiB_2 is $c_0 = 0.3220$ nm [85]. Thus, the $TiB_{2.4}$ films exhibit compressive macrostrain in the as-deposited state ($c > c_0$), changing to an essentially unstrained condition after annealing at $T_a \geq 700$ °C (see Fig. 1b). The full-width-at-half-maximum intensity Γ_{0001} of the (0001) reflection remains constant at $0.28 \pm 0.01°$ as a function of annealing temperature for $T_a \leq 800$ °C (Fig. 1b) suggesting that there are no significant changes in either nanostructure or local lattice microstrain [89] as a function of annealing.

Increased diffusivities during film annealing commonly lead to defect annihilation and atomic rearrangement, resulting in lower stresses [73, 90]. Since structural defects act as obstacles for dislocation motion, a direct relationship between defect density and hardness is expected [73]. Thus, lattice parameter, diffraction peak widths Γ, and the hardness of stoichiometric binary nitride and carbide layers typically decrease during annealing [17–38]. This is shown in Fig. 2 for TiN layers deposited at 300 °C, which exhibit intrinsic compressive macrostrain (due to built-in growth-defects) in the as-deposited state ($a > a_0$) changing to an almost unstrained condition after annealing at $T_a \geq 800$ °C (see Fig. 2). In addition to a, also the diffraction peak widths Γ (only Γ_{200} is shown, although the TiN films have a random orientation) decrease with T_a for annealing at tem-

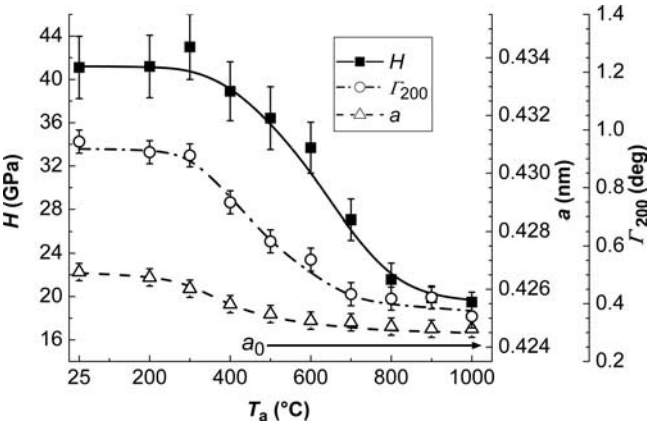

Fig. 2. Hardness H, lattice parameter a, and full-width-at-half-maximum intensity Γ of the (200) XRD reflection of TiN films as a function of T_a, the annealing time was 1h. For comparison, the lattice parameter a_0 of TiN is indicated by an arrow.

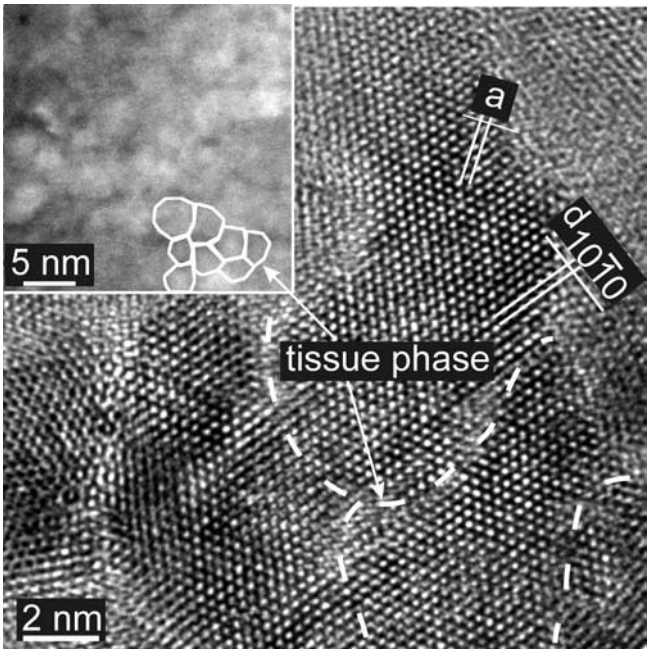

Fig. 3. Bright-field plan-view (0001) HRTEM image of an as-deposited $TiB_{2.4}$ layer. The insert is a lower-resolution Z-contrast image.

peratures above the deposition temperature. The results suggest that the increased diffusivities lead to defect annihilation and atomic rearrangement, resulting in less defects and lower stresses. Consequently, the hardness of the films approaches the hardness for bulk TiN ($H \sim 20$ GPa [91]) as the growth-defect hardening diminishes. However, for overstoichiometric $TiB_{2.4}$, it is shown that while the film lattice constant (and hence macrostress) decreases with annealing temperature $T_a \leq 800\,°C$, Γ and H remain constant (see Fig. 1b) [78].

TEM investigations reveal no observable differences in the nanostructure of as-deposited $TiB_{2.4}$ layers and samples which were annealed at 700 °C [78]. This is consistent with the XRD results showing that Γ_{0001} remains constant with T_a. As confirmed by HRTEM and high-angle annular dark-field (Z-contrast) investigations, superhard overstoichiometric TiB_2 films have a columnar structure, with an average size of ~ 20 nm, and (0001) preferred orientation. The columns are encapsulated in excess B and are themselves composed of smaller stoichiometric TiB_2 subcolumns with an average diameter of ~ 5 nm, separated by a thin B-rich tissue phase of thickness 1–2 ML (see the plan-view HRTEM image in Fig. 3). The insert in Fig. 3 is a high-angle annular dark-field (Z-contrast) plan-view image where ~ 5 nm sized bright areas are embedded in darker areas (elucidated by white lines). Regions with lower average atomic number Z appear darker and are therefore B-rich compared to the brighter TiB_2 regions. Thus, the nanostructure of $TiB_{2.4}$ is composed of bundles of ~ 5 nm diameter coherent subcolumns, separated by a thin (~ 0.5 nm, 1–2 ML) disordered B-rich tissue phase. This substructure is located within ~ 20 nm wide (0001)-oriented columns [78]. Quantitative analyses of electron energy-loss spectroscopy (EELS) measurements obtained from plan-view samples using a 1 nm spot size reveal that the subcolumns are stoichiometric TiB_2, whereas the disordered regions are highly B-rich with a B/Ti at.% ratio > 2 [78].

Due to the small dimension across the TiB_2 nanocolumns (i. e., the (0001) plane, which is also the primary dislocation glide plane [78]), nucleation and glide of dislocations is inhibited during hardness indentation measurements, while the high cohesive strength of the thin B-rich tissue phase prevents grain-boundary sliding. Together, these two effects explain the observed superhardness of overstoichiometric TiB_2 layers. As a consequence of the thermal stability of this nanostructure, also the hardness is unaffected for $T_a \leq 800\,°C$.

3.1.2. Three-dimensional nanostructure of TiN–TiB_2

An example to obtain a three-dimensional nanostructure is given for a TiN–TiB_2 thin film, which is non-reactively co-sputtered from a segmented TiN–TiB_2 target [16, 79]. The bright-field cross-sectional HRTEM micrograph in Fig. 4a shows randomly oriented 2–3 nm sized crystals of the layer in the as-deposited state. The Z-contrast image (Fig. 4b) clearly indicates a random orientation over the whole film of at least two different phases (brighter and darker dots). The brighter dots indicate the appearance of a phase with a higher density (Z) than compared to the phase represented by the darker dots. It is shown in Ref. [79] that although the chemical composition of the film with 38 at.% Ti, 30.5 at.% B, and 31.5 at.% N is located in the TiN–TiB_2–BN ternary phase field of the equilibrium Ti–B–N phase diagram, the film only consists of stoichiometric TiN and TiB_2 crystals encapsulated by B-rich disordered regions. There is no evidence of crystalline BN.

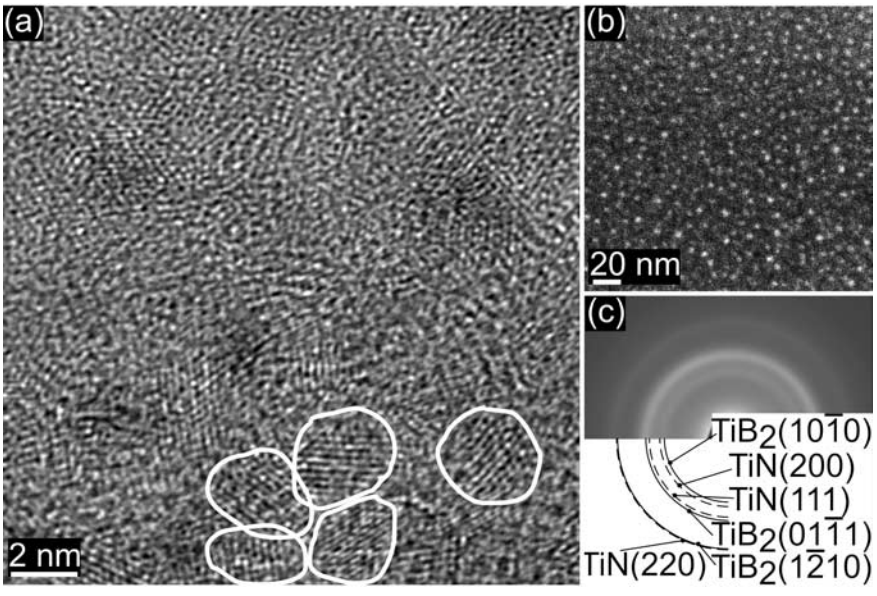

Fig. 4. (a) Cross-sectional bright-field HRTEM image of a TiN–TiB_2 film, (b) Z-contrast image indicating at least two different phases, (c) SAED pattern with fcc-TiN and hcp-TiB_2 standard diffraction rings.

The diffraction rings in Fig. 4c indicate a mixture of TiN and TiB_2 nanocrystals with random orientation and a

considerable amount of disordered regions. Due to the limited local resolution and a possible lattice deformation, no clear relation to the individual phases is possible. Considering the extremely short diffusion path for point and line defects in 2–3 nm grains to the nearest sink (i. e., grain and phase boundaries, interfaces), almost *perfect* crystals should form during deposition. Therefore, the film mainly consists of TiB_2 and TiN crystals with low defect density. In such nanocomposites with an average grain size of about 2–3 nm, the volume fraction of disordered grain and phase boundaries is in the range of ~ 70 % [39]. Furthermore, excess boron, which is known to segregate easily to boundaries, favors the formation of B-rich disordered boundary regions [92]. But also the formation of amorphous BN surrounding the nanocrystals is likely [9, 93]. However, these disordered boundary regions and the small grain size of 2–3 nm are responsible for an increased interfacial volume fraction, explaining the contribution of amorphous-like diffraction rings to the selected-area electron diffraction (SAED) pattern (see Fig. 4c).

The structural evolution with annealing at different temperatures of the TiN–TiB_2 film is shown in Fig. 5, represented by XRD patterns. The steel substrate reflections are at 43.62° and 74.70° [94]. In the as-deposited state, the broad film XRD peaks are the result of overlapped broad TiN and TiB_2 reflections. Such broad reflections indicate small grain sizes and/or high lattice strains of a crystalline phase but also a huge amount of disordered regions [89]. This is in agreement with HRTEM and SAED investigations (Figs. 4a and c) of the TiN–TiB_2 film in the as-deposited state. Likewise, also from XRD investigations no evidence for crystalline BN can be found. The high hardness value of ~ 42 GPa for as-deposited films (Fig. 6a) emphasizes also the absence of hexagonal BN. After annealing, the two phases TiN and TiB_2 become more pronounced, indicated by their separated XRD peaks for $T_a \geq 800$ °C. This indicates an occurring crystal growth, which consequently reduces the disordered boundary fraction (i. e., interfacial fraction), due to increased diffusivity at higher temperatures. After annealing at $T_a \geq 1000$ °C, more TiN and TiB_2 reflections can be detected by XRD, indicating that recrystallization occurs [73]. A fully recrystallized structure, containing TiN and TiB_2 phases, can be seen for $T_a = 1400$ °C. Corresponding to the nanostructural changes within the film during annealing, also the hardness H and the reduced elastic modulus E^* ($E^* = E \cdot (1-\nu^2)^{-1}$, where E is the elastic modulus and ν is the Poisson ratio) change with T_a (see Fig. 6a). An increase of H from ~ 42 to ~ 52 GPa is achieved by an annealing treatment up to 800 °C. If T_a exceeds 900 °C, the hardness of the film decreases again, but a hardness value of ~ 42 GPa after annealing at 1000 °C is still extraordinary high for thin films [17]. E^* slightly increases from ~ 352 GPa in the as-deposited state to ~ 405 GPa after annealing at $T_a \geq 900$ °C. The average grain size d of TiN and TiB_2 crystals is 2–3 nm for $T_a \leq 800$ °C and increases for $T_a > 900$ °C (see Fig. 6b). In addition to HRTEM investigations [79], the average crystallite size d of the films is estimated from single-line profile analyses of XRD patterns fitted with Cauchy functions [89] with peak maxima at TiN and TiB_2 diffraction positions, as the film is composed

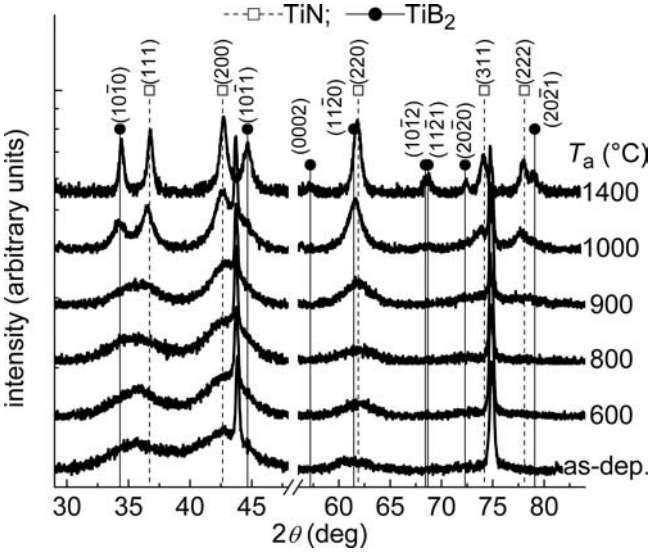

Fig. 5. XRD evolution of a TiN–TiB_2 film with annealing temperature T_a, the annealing time was 30 min.

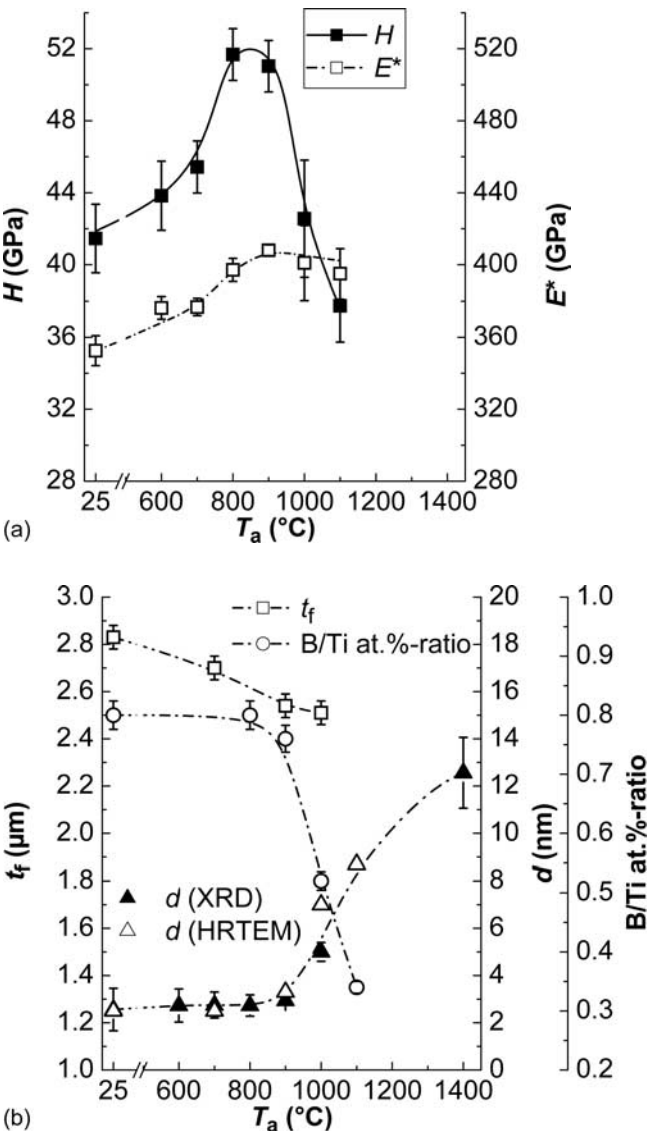

Fig. 6. (a) Hardness H and reduced elastic modulus E^* ($E^* = E \cdot (1-\nu^2)^{-1}$), (b) film-thickness t_f, B/Ti at.%-ratio and average grain size d (obtained from XRD patterns and HRTEM images) of the TiN–TiB_2 film with annealing temperature T_a, the annealing time was 30 min.

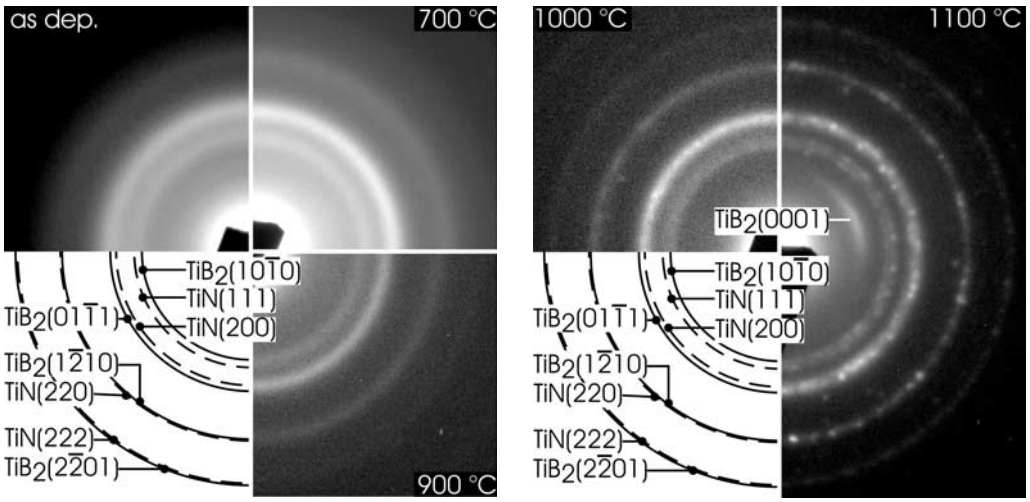

Fig. 7. Development of the SAED diffraction rings of a TiN–TiB_2 film with T_a, the annealing time was 30 min. The standard diffraction rings for fcc-TiN and hcp-TiB_2 are added.

of nearly *defect-free* TiN and TiB_2 nanocrystals [79]. The *d* values obtained from HRTEM and XRD match each other very well (see Fig. 6b).

Film-thickness t_f values (see Fig. 6b) are obtained from cross-sectional HRTEM investigations where one deposited sample is cut into pieces which are then individually annealed at T_a. These values decrease from 2.83 µm (as-deposited) to 2.51 µm (T_a = 1000 °C), indicating that the annealing gives rise to compact boundary regions and reduction of their volume fraction [95] for $T_a \leq 800$ °C (see Fig. 6b). Since no additional phases are formed during the annealing treatments (Fig. 5), the increased hardness for $T_a \leq 900$ °C is related to the nanostructural rearrangement and the formation of compact boundary regions due to increased diffusivity (see Fig. 6). Therefore, also the reduced elastic modulus E^* increases slightly (see Fig. 6a) [96]. The boron content of the TiN–TiB_2 film decreases if $T_a \geq 900$ °C, causing a reduction of the B/Ti at.% ratio (see Fig. 6b), whereas the N/Ti at.% ratio remains constant at ~0.83 with $T_a \leq 1100$ °C. During annealing at 1100 °C, the B/Ti at.% ratio changes from 0.80 to ~0.35. This loss of B during annealing at $T_a \geq 900$ °C for TiN–TiB_2 thin films [79] on stainless steel is attributed to the formation of volatile B-oxides with residual oxygen of the annealing atmosphere [93].

Due to the reduction of the boron content, the TiN–TiB_2 film meets the quasi-binary TiN–TiB_2 tie line of the Ti–B–N equilibrium phase diagram after annealing at T_a = 1100 °C. As-deposited, the chemical composition is within the ternary TiN–TiB_2–BN phase field, but SAED and XRD investigations show no evidence for a crystalline BN phase. Also, during annealing at $T_a \leq 1400$ °C no crystalline BN phase is formed. This indicates that the films have B-rich (or amorphous BN and amorphous TiB_x containing) [9, 93] interfaces, and hence an increased disordered volume fraction and small (i. e., 2–3 nm) crystals [92]. But due to the high cohesive strength of B-containing boundaries [97], the film is extremely hard, regardless of the high disordered boundary fraction. The results of the structural investigations indicate that B-rich boundary regions inhibit grain growth and recrystallization. As a consequence, the effectiveness in hindering grain growth and recrystallization decreases with the B-content [16]. For the film composition investigated here, at $T_a \geq 1000$ °C clearly separated TiN and TiB_2 XRD peaks can be seen, due to the increased crystallite size, which results in a hardness decrease (compare Figs. 5 and 6).

The SAED investigations of the film in the as-deposited state and after different annealing treatments (Fig. 7) show corresponding results to XRD. The as-deposited film shows diffuse SAED rings due to a high fraction of disordered regions and 2–3 nm sized TiN and TiB_2 crystals with random orientation, as discussed above. With increasing temperature, these diffuse diffraction rings become gradually sharper indicating a reduction of the volume fraction of disordered regions (i. e., interfaces) and a slight increase in grain size of the nanocrystals. At 900 °C, the diffraction rings match the standard TiN and TiB_2 rings, but still it cannot be distinguished between these two different phases due to their small crystallite size [79]. The SAED patterns of samples after annealing at 1000 °C and 1100 °C indicate a further growth of the TiN and TiB_2 phases. Especially for T_a = 1100 °C, separate diffraction rings of TiN and TiB_2 with small discrete spots can be identified. In agreement with the XRD and HRTEM investigations [79], the SAED patterns show that the films start to recrystallize if the annealing temperature exceeds 1000 °C.

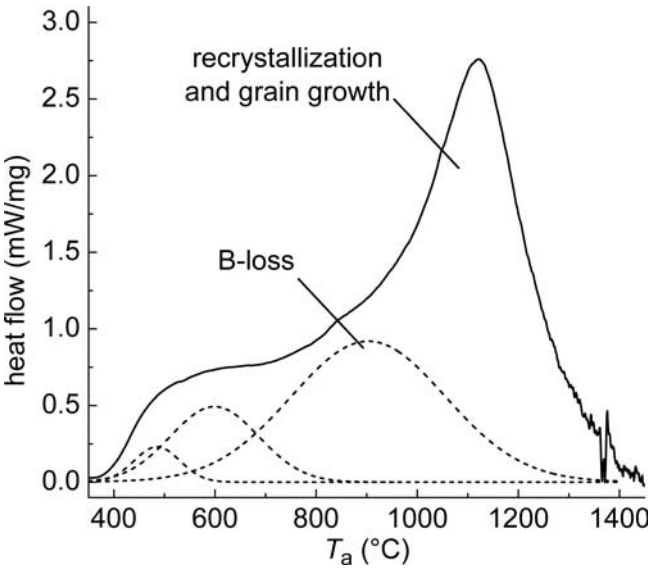

Fig. 8. Dynamical DSC measurement of a TiN–TiB_2 film, showing a huge exothermic reaction due to recrystallization and grain growth. Additional exothermic reactions are indicated by dashed lines.

Dynamical DSC measurements of TiN–TiB_2 films clearly show several exothermic reactions that superpose themselves during annealing in Ar up to 1400 °C (see Fig. 8). By comparing the DSC results with XRD, HRTEM, SAED and EPMA investigations of the films after different annealing temperatures, it can be concluded that the exothermic reactions at temperatures ≤ 800 °C are due to recovery effects and the formation of compact B-rich boundary regions. The exothermic reaction with a peak temperature of ~ 900 °C, indicated in Fig. 8, is mainly due to the loss of B (compare Fig. 6b), by the formation of volatile B-oxides with residual oxygen from the annealing atmosphere [93]. No other structural modifications are present. Accumulation effects of atoms from the disordered boundary regions to the encapsulated TiN and TiB_2 crystals contribute to the exothermic reactions at $T < 900$ °C. The huge exothermic reaction with a peak temperature of ~ 1150 °C is due to the occurring recrystallization and grain growth processes [12, 16], promoted by a reduction of disordered boundary regions as the B-content decreases in the TiN–TiB_2 films. Consequently, the film-hardness decreases (see Fig. 6a). The structural and chemical modifications result in a reduction of the total free energy of the films, causing exothermic signals during DSC measurements.

3.2. Nanostructures generated during annealing

During annealing of supersaturated phases, coherent and/or semi-coherent precipitates form that provide a substantial strengthening effect [64, 98, 99]. Coherency strains between matrix and coherent small domains as well as the precipitates themselves influence dislocation generation and motion [98]. As soon as the equilibrium phase precipitates and grows at constant volume fraction, the hardness decreases as less obstacles (and hence interfaces) are available. This decomposition process via the formation of intermediate phases is shown for two supersaturated films, Ti(B)N and $Ti_{0.33}Al_{0.67}N$, generated by vapor deposition. Both films show as-deposited a dense columnar microstructure of a supersaturated NaCl-structured phase based on fcc-TiN. For Ti(B)N, the non-metallic part (N) of the TiN lattice is substituted by B [80], whereas for $Ti_{0.34}Al_{0.66}N$, the metallic part (Ti) of the TiN lattice is substituted by Al [26–34, 37]. For comparison, $TiB_{2.4}$ and TiN–TiB_2 (discussed above) and similar nanocomposite thin-film materials that also attract a large interest [19, 24, 100–102] cannot undergo such transformation during annealing as they are equilibrium-phase materials already in the as-deposited state.

3.2.1. Decomposition of supersaturated Ti(B)N

In the as-deposited state, the Ti(B)N film contains 43.4 at.% Ti, 3.2 at.% Cl (which is due to the utilization of $TiCl_4$ and BCl_3 precursors in the PACVD process [3]), 17.4 at.% B and 36.0 at.% N. The film is close to the quasibinary TiN–TiB_2 tie line of the ternary Ti–B–N phase diagram. Experimental (i. e., EPMA and XRD) and *ab initio* [103, 104] results [80] show that the Ti(B)N film is composed of a metastable NaCl-structured Ti(B)N phase where B substitutes N, and excess B is located at grain boundaries. The Cl atoms are mainly situated at the grain boundaries, thereby reducing their cohesive strength [105], and are partly incorporated into the lattice [3].

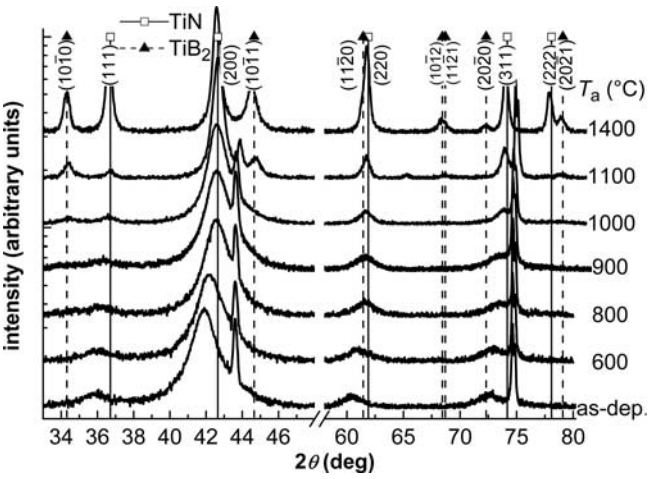

Fig. 9. XRD patterns of an as-deposited Ti(B)N film and samples which have been annealed for 30 min at temperatures T_a.

Figure 9 indicates that the XRD film-peak positions shift towards the standard values of stoichimetric TiN during annealing at $T_a < 800$ °C. The steel substrate reflections are at 43.62° and 74.70° [94]. After annealing at $T_a = 800$ °C, where the XRD film-peak positions are close to those of stoichiometric TiN, an additional small XRD reflection at ~ 34.34° can be detected (see Fig. 9). This peak, which matches (10$\bar{1}$0) TiB_2, gradually increases (and hence the TiB_2 fraction) as the film is annealed at higher temperatures. The XRD results show that additional reflections of the hcp-TiB_2 phase can be detected for $T_a \geq 800$ °C. After annealing the film at $T_a \geq 1100$ °C, the preferred (10$\bar{1}$0) orientation of the precipitated TiB_2 phase and the preferred (200) orientation of the film-matrix change into a more random orientation (Fig. 9). This loss in preferred orientation of precipitate and film-matrix indicates the onset of recrystallization effects of the Ti(B)N film. The temperature fits to investigations concerning the recrystallization of Ti–B–N films [16]. Annealing treatment at 1100 °C and subsequent rapid cooling to room temperature cause also structural changes of the steel substrate. The substrate XRD peak positions slightly shift from 43.62° to 43.83° and from 74.70° to 75.01°, and also additional reflections at 44.69° and 65.25° can be detected, which match with the Ni–Cr–Fe phase [94]. The Ti(B)N film is fully recrystallized with fcc-TiN and hcp-TiB_2 phases in random orientation after annealing at $T_a = 1400$ °C (Fig. 9).

The decomposition process of the supersaturated Ti(B)N phase to form TiB_2 can be explained in more detail from the influence of T_a on the lattice parameter a and the full-width-at-half-maximum intensity Γ_{200} of the film-matrix (200) reflection (Fig. 10). Fig. 10 shows that the lattice parameter a is about 0.4315 nm for $T_a \leq 500$ °C and gradually decreases from 0.4315 to 0.4245 nm ($a_0 = 0.4240$ nm for bulk TiN) after annealing between 500 °C and 800 °C, respectively (see Fig. 10). The B/Ti film ratio is unaffected by the annealing treatments at $T_a \leq 1100$ °C. Consequently, the decreasing lattice parameter suggests that the B-solute concentrations of the film matrix decreases from the as-depasited condition to zero. As-deposited the B-solute *and* excess B at grain boundaries is ~ 17.4 at.%. Chlorine dif-

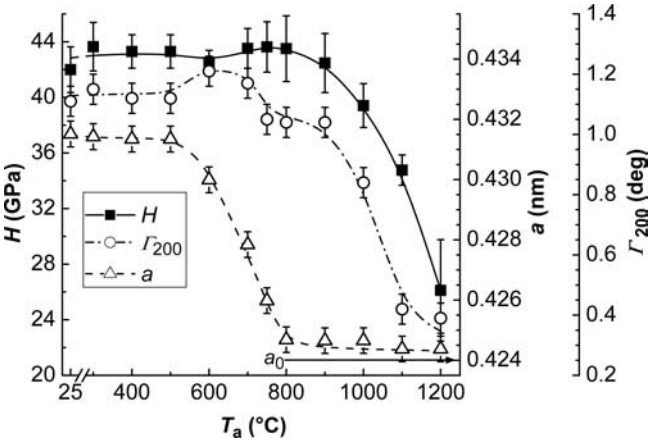

Fig. 10. Hardness H, lattice parameter a, and full width at half maximum intensity Γ_{200} of the (200) XRD reflection of the Ti(B)N film-matrix as a function of T_a, the annealing time was 30 min. For comparison, the lattice parameter a_0 of TiN is indicated by an arrow.

fuses out of the films if annealed at temperatures above 700 °C, corresponding results are also obtained by mass-spectroscopy measurements during annealing of Cl containing TiN films [106]. At $T_a = 1100$ °C the Cl content of the films is essentially zero.

The full-width-at-half-maximum intensity Γ_{200} of the (200) reflection remains constant at $1.12 \pm 0.02°$ as a function of annealing temperature for $T_a \leq 500$ °C (Fig. 10), suggesting that there are no significant changes in either nanostructure or local lattice microstrain [89]. But as soon as T_a is higher than the growth temperature and the B-solute concentration of the film-matrix decreases, Γ_{200} increases to ~ 1.20° and is above 1.05° unless T_a exceeds 900 °C (Fig. 10). Consequently, the local lattice microstrains should decrease (and hence Γ_{200}). This behavior indicates that, due to the decomposition process of the metastable Ti(B)N phase, coherent and/or semi-coherent B-rich metastable phases are formed, which contribute to Γ_{200}, if T_a is between 500 and 900 °C. Annealing the film at $T_a \geq 1000$ °C causes a gradual decrease of Γ_{200} from 1.05° at $T_a = 1000$ °C to 0.29° at $T_a = 1400$ °C. Increasing the annealing temperature from 900 to 1200 °C causes also an increasing fraction of incoherent hcp-TiB_2 precipitates, which start to form at ~ 800 °C (see Fig. 9). Thus, the XRD results of annealed Ti(B)N films (Figs. 9 and 10) indicate that the coherent and/or semi-coherent metastable B-rich phases, which start to form at ~ 500 °C, when the B-solute concentration of the film matrix decreases, gradually transform into incoherent hcp-TiB_2 with T_a.

In the as-deposited state, the Ti(B)N film hardness is at a very high value of 42 ± 2 GPa due to the small grain size, growth-defects, solid-solution hardening, and excess B which is located at grain boundaries and thereby increases their cohesive strength [78, 97]. The hardness for bulk stoichiometric TiN is ~ 20 GPa. The Ti(B)N film-hardness remains at ~ 43 GPa for $T_a \leq 900$ °C, although the growth-defect density and the concentration of solute B-atoms in the film-matrix (and hence the lattice parameter a) decrease if the annealing temperature exceedes the deposition temperature (see Fig. 10). Thus, the decreasing growth-defect and solid-solution hardening effects are compensated by the onset of age hardening, as simultaneously B-rich precipitates are formed. The film-hardness decreases as the fine-dispersed particles grow. When the TiB_2 precipitates grow at constant volume fraction, the decreasing number of particles and the concomitant increase in mean intercenter spacing between particles result in decreasing particle-strengthening and hence decreasing film-hardness (see Figs. 9 and 10 for $T_a \geq 1000$ °C).

3.2.2. Decomposition of supersaturated $Ti_{0.33}Al_{0.67}N$

Figure 11a shows the hardness of $Ti_{0.33}Al_{0.67}N$ as a function of T_a. A hardness increase between 600 and 950 °C occurs, indicating age-hardening effects. These age-hardening effects cannot occur for films with large single-phase fields like TiN [38], where a decrease in hardness at temperatures higher than the deposition temperature occurs (see Fig. 2) due to recovery and recrystallization [36–38]. For comparison with the $Ti_{0.33}Al_{0.67}N$ film, the hardness as a function of T_a for an arc-evaporated TiN film grown at 500 °C is shown in Fig. 11a.

Age-hardening causes microstructural changes in the films, where the related changes in total free-energy can be detected by DSC. During heating of the supersaturated $Ti_{0.33}Al_{0.67}N$ film, four exothermic reactions occur (see Fig. 11b). Clarification of the origin of these reactions is obtained by XRD investigations of films annealed slightly beyond the corresponding peak temperature (see Fig. 12).

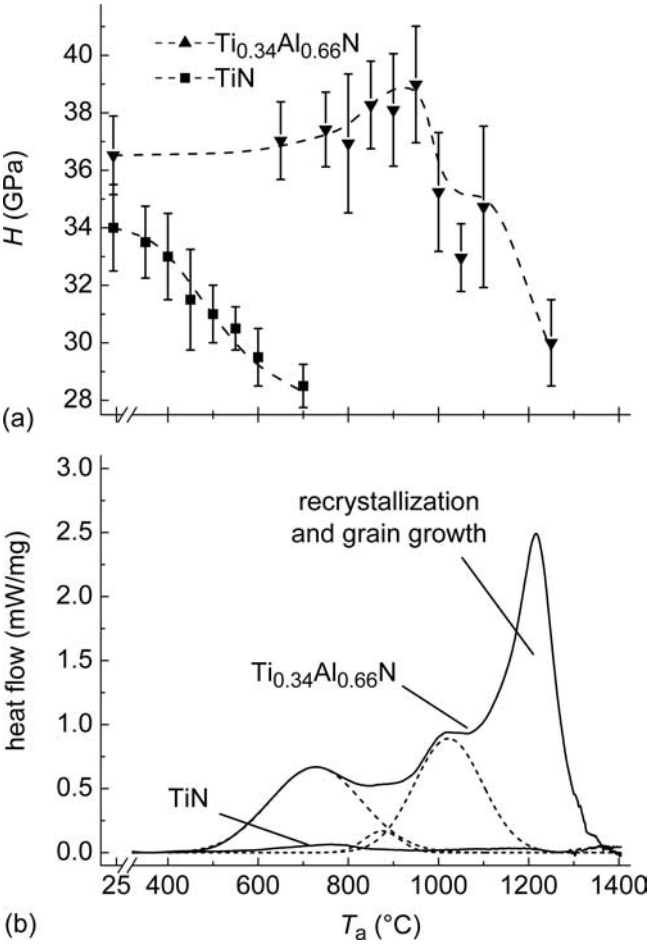

Fig. 11. (a) Hardness H as a function of T_a (annealing time was 120 min) and (b) Dynamical DSC measurements of $Ti_{0.33}Al_{0.67}N$ and TiN.

Since the layers were previously removed from their substrates, any substrate-reaction was eliminated. The exothermic reaction at ~ 720 °C is due to recovery and structural reordering of the supersaturated $Ti_{0.33}Al_{0.67}N$ phase [17, 37]. Comparison of XRD patterns of the as-deposited condition and after annealing at T_a = 760 °C shows that in the films only recovery processes occurred [17]. After T_a = 890 °C, an increase of the right-hand shoulder (close to fcc-AlN) of the (200) peak was found. The XRD peak can no longer be described by one symmetric function, indicating the formation of AlN-rich domains (see Fig. 12). The coherency strains cause a shift of the XRD matrix-peak to the position of fcc-AlN and vice versa [17]. The newly formed domains and the coherency strains cause the hardness to increase (see Fig. 11a) by influencing the generation and motion of dislocations.

After T_a = 1030 °C, the films are composed of three different phases (see Fig. 12): fcc-$Ti_{1-x}Al_xN$ (matrix), fcc-TiN, and fcc-AlN. The AlN-rich domains which were most probably formed by spinodal decomposition [98, 99] (T_a = 890 °C) coarsened to separate phases resulting in a hardness decrease (see Fig. 11a), which is retarded by the formation of TiN-rich domains at T_a = 1030 °C. After annealing at T_a = 1400 °C, the decomposition process is completed and the fcc-AlN phase transformed into its stable hcp structure. XRD indicates that the $Ti_{0.33}Al_{0.67}N$ films are now composed of fcc-TiN and hcp-AlN phases (see Fig. 12). Thus, the reaction at ~ 1210 °C, which is due to film-recrystallization including the transformation of fcc-AlN into its stable hcp form [17, 37], causes the hardness to decrease (see Fig. 11a). The possible phase transformations in this system are further assessed by experimental results [107] and *ab initio* studies [17, 108, 109].

For TiN, just one small exothermic reaction at ~ 750 °C can be detected by DSC. XRD and TEM investigations, prior to and after this exothermic reaction of TiN, indicated recovery processes of deposition-induced lattice point defects [37]. Such structural relaxations explain the hardness decrease at temperatures above the growth temperature (see Fig. 2 and Fig. 11a) [36, 37].

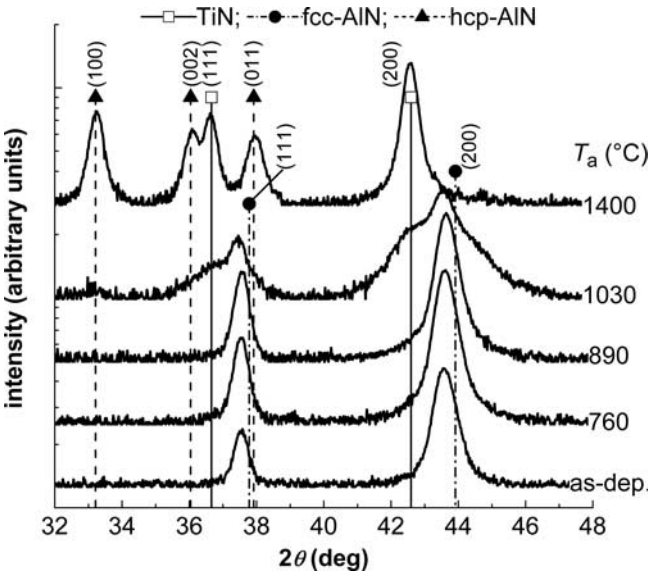

Fig. 12. XRD evolution of a $Ti_{0.33}Al_{0.67}N$ film with annealing temperature T_a, the annealing time was 120 min.

4. Discussion

Growth of overstoichiometric TiB_2 films results in the formation of a dense columnar structure with an average size of ~ 20 nm, and (0001) preferred orientation. Although the film presented here is sputtered from a stoichiometric TiB_2 target in a pure Ar discharge, its chemical composition is overstoichiometric with B/Ti = 2.4. A detailed explanation for this unusual behavior, which is also observed by other research groups [13, 14, 25, 82, 110–115], is still missing. Investigations on how the B/Ti ratio is influenced by the deposition conditions showed that increasing the Ar pressure results in a reduction of the B/Ti ratio, even below 2 [110]. This would explain the observed hardness decrease with increasing Ar pressure [116], as excess B (and hence a B/Ti ratio > 2) is necessary for the formation of a nanocolumnar structure [78]. Increasing the target-to-substrate distance or using Xe instead of Ar as the sputtering gas also results in a B/Ti ratio below 2 [110]. An increasing B/Ti ratio, even above 3, is found for increasing J_{Ar+}/J_{Ti} [78]. For rf-sputtered films, an increase of B/Ti from 2.1 to 2.8 with increasing the negative bias voltage from 0 to −50 V, respectively, occurred [115].

As TiB_2 has a relatively narrow single-phase field (65.6 to 66.7 at.% B), the excess B in our $TiB_{2.4}$ films segregated to interfaces. Due to the limited diffusivity at the low deposition temperature of 300 °C, B that cannot reach the column boundaries, accumulates to form a tissue phase within the columns (see Fig. 13). This process is preferred along the (0001) plane as this is the preferred B-diffusion plane in TiB_2. Consequently, columns are encapsulated in excess B and are themselves composed of smaller stoichiometric TiB_2 subcolumns with an average diameter of ~ 5 nm, separated by a thin B-rich tissue phase of thickness 1–2 ML. Due to the small dimension across the TiB_2 nanocolumns, nucleation and glide of dislocations is inhibited during hardness indentation measurements (the primary dislocation glide plane in TiB_2 is (0001)), while the high cohesive strength of the thin B-rich tissue phase prevents grain-boundary sliding. Together, these two effects explain the observed superhardness of overstoichiometric TiB_2 layers.

Sputtering of a ceramic TiN–TiB_2 target causes a flux of Ti, N, and B atoms arriving on the substrate, resulting in the formation of TiN and TiB_2 nuclei (see Fig. 14). Boron has a low solubility in TiN and segregates during film growth to surfaces and interfaces, forming B-rich disordered regions which cover TiN surfaces and reduce boundary mobility.

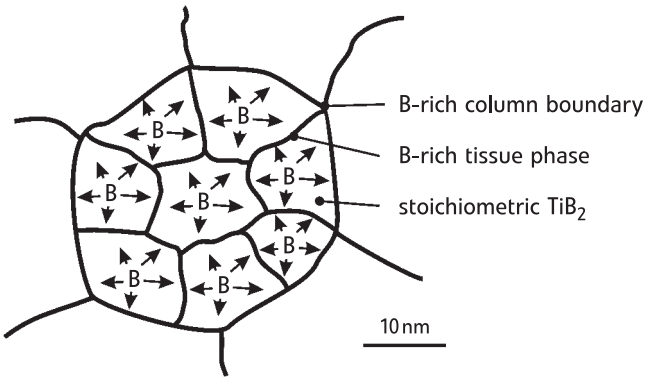

Fig. 13. Schematic cross-section of the (0001)-textured ~ 20 nm wide columns, indicating the generation process of the B-rich tissue phase by preferred B-diffusion on the (0001) plane.

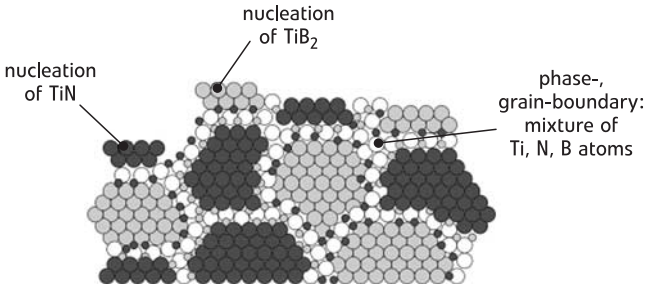

Fig. 14. Schematic nucleation process of TiN–TiB_2, indicating segregation-driven re-nucleation of TiN and TiB_2.

The presence of these regions affects film growth and hinders grain coarsening during coalescence and further grain growth [117, 118]. The B-enriched areas, covering TiN crystals, promote nucleation of TiB_2, which itself has a low solubility for N. Thus, similar segregation-driven processes occur for N with TiB_2 as mentioned above for B with TiN. These processes periodically interrupt the epitaxial growth of individual crystallites and cause renucleation, as indicated in Fig. 14. The periodically interrupted growth explains the extremely small crystallite size of 2–3 nm for TiN–TiB_2 films. The observed results, that the film hardness increases, and also the reduced elastic modulus increases, the film thickness decreases, and the grain size slightly increases with $T_a \leq 900\,°C$ (see Fig. 6), indicate that the annealing gives rise to compact boundary regions and a reduction of their volume fraction [95]. Thus, in the as-deposited state, the interfacial volume fraction is too high for peak-hardness, or the crystallite size is below the critical grain size d_c where the Hall–Petch effect ceases or even reverses [67, 119].

Yip [119] describes d_c as the smallest size that can sustain a dislocation pile-up. Below this size, dislocation blocking breaks down and intergranular sliding becomes important, as the proportion of interfacial atoms increases. Thus, the constitution of interfaces themselves plays an important role in determining the properties of such materials. The mechanical properties of many materials can be increased by additions of B, which was proven to enhance the cohesion of boundaries by affecting the local bonding at the interface [120, 121]. This agrees with our results where TiN–TiB_2 films with B-rich interfaces, although having extremely small grains of 2–3 nm in the as-deposited state, exhibit a high hardness of ~ 42 GPa.

Post-annealing of the films gives rise to compact interfaces and crystallites of ~ 3 nm for $T_a = 900\,°C$ [79]. Therefore the film-hardness increases and also the reduced elastic modulus increases slightly with T_a (see Fig. 6a). A schematic representation of the nanostructural modification during annealing of the TiN–TiB_2 film is given in Fig. 15 [79]. Annealing the TiN–TiB_2 films in vacuum at temperatures $T_a \leq 900\,°C$ causes the formation of compact boundaries, resulting in a hardness increase (see Fig. 6a). XRD (Fig. 5) and SAED (Fig. 7) investigations show a reduction of the disordered (interfacial) regions in the films for $T_a \leq 900\,°C$, which is fostered by decreasing film-thickness (Fig. 6b). As soon as the B content decreases (see Fig. 6b), the volume fraction of disordered regions decreases, the grain size increases (see Figs. 6b and 8 for $T_a \geq 900\,°C$) and consequently the hardness decreases (compare Figs. 5, 6, 7, and

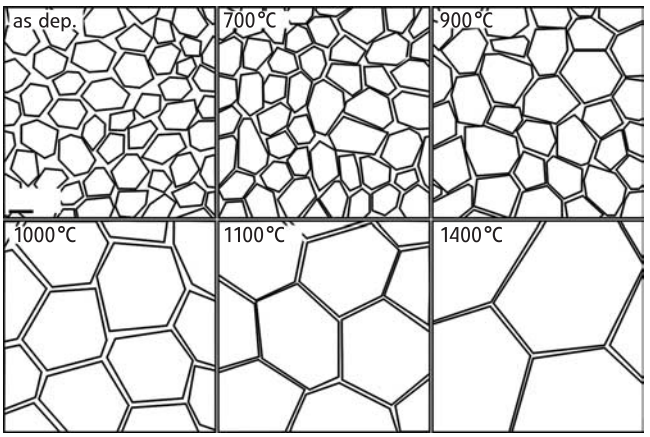

Fig. 15. Schematic representation of the evolution of nanostructure with annealing temperature T_a for a TiN–TiB_2 film.

15). After annealing the film at 1400 °C, a fully recrystallized and two-phase structure composed of TiN and TiB_2 crystals is formed.

Contrary to TiN–TiB_2 films with 30.5 at.% B, which have a nanostructural arrangement of the equilibrium phases TiN and TiB_2 already in the as-deposited state, Ti(B)N films containing 17.4 at.% B grow with a dense columnar microstructure of a supersaturated TiN phase, where B substitutes N. During annealing, the supersaturated phase initially undergoes decomposition into coherent and/or semi-coherent B-rich domains, causing an increase in hardness at elevated temperatures. The generation of domains is schematically illustrated in Fig. 16a. If a domain is formed with a lattice parameter (a_β) different from the matrix (a_α), both domain and matrix must be strained by equal and opposite forces for full coherency. Therefore, the hardness increases as additional stress is required to propagate dislocations through these domains. Adequate mechanisms occur for $Ti_{0.33}Al_{0.67}N$, which show a supersaturated TiN-based phase, where Al substitutes Ti. The decreasing growth-induced and solid-solution hardening effects during annealing at temperatures above the growth temperature are compensated or even more than compensated by the onset of precipitation hardening for both systems. The film-hardness decreases as the fine-dispersed particles grow. When the

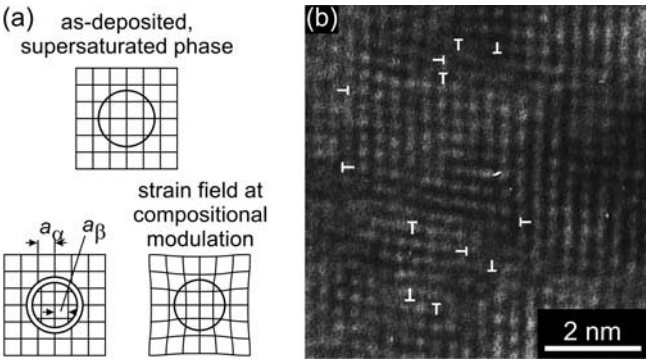

Fig. 16. (a) Schematic drawing showing the origin of coherency strains. The lattice parameters of the matrix and the newly formed domain are indicated by a_α and a_β, respectively. (b) HRTEM micrograph showing the [001] projection of an fcc-$Ti_{0.33}Al_{0.67}N$ lattice with dissociated {110}<110> misfit dislocations due to relaxation of coherency strains.

precipitates grow at constant volume fraction, the decreasing number of particles and the concomitant increase in mean intercenter spacing between particles result in decreasing particle-strengthening and hence decreasing film-hardness.

The findings for $Ti_{0.33}Al_{0.67}N$ point to a coherency of the formed AlN-rich and TiN-rich domains. Verification is obtained by HRTEM showing strained domains. After annealing at 1100 °C, the coherency strain between fcc Ti-rich and Al-rich domains became relaxed by the introduction of misfit dislocations, as shown in Fig. 16b [17].

5. Conclusion and outlook

The hardness of a material is determined by its resistance to bond distortion and to dislocation formation and motion, which themselves depend on the amount of interfaces and their constitution. Consequently, there is a direct relation between hardness and the nanostructure of materials. Nanostructures can arise in thin films during growth by plasma-assisted vapor deposition or during post-annealing treatments if they contain supersaturated metastable phases.

An example for a two-dimensional nanostructure is given for overstoichiometric (0001)-textured columnar TiB_2 films, where excess B forms an ultra-thin B-rich tissue phase during growth, separating ~ 5 nm diameter TiB_2 subcolumns. During post-annealing at temperatures exceeding the growth temperature, where growth-defect hardening diminishes due to defect annihilation and atomic rearrangement, the hardness for $TiB_{2.4}$ remains at ~ 60 GPa as its columnar nanostructure is unaffected by the heat treatment. This is in contrast to 30.5 at.% B containing TiN – TiB_2 thin films, where randomly orientated 2 – 3 nm sized TiN and TiB_2 crystals, generated by segregation-driven renucleation, are embedded in a B-rich disordered interfacial fraction. Post-annealing of these films gives rise to compact internal boundaries (interfaces) and increases the crystallite sizes to ~ 5 nm. Consequently, their hardness increases as the interfacial volume fraction slightly decreases, and also the resistance against bond distortion of the interfaces increases. During annealing at $T_a \geq 900$ °C, the B content of the films decreases due to the formation of volatile B-oxides with residual oxygen of the annealing atmosphere. This loss in B is at the expense of the disordered boundary fraction which inhibits grain growth and recrystallization, which start during annealing at $T_a > 1000$ °C resulting in a hardness decrease.

Growth of 17.4 at.% B containing Ti(B)N films results in a columnar, single-phased supersaturated TiN structure, where B substitutes N. Annealing of the layers at temperatures above the growth temperature causes a decomposition of the supersaturated phase and hence the formation of B-rich domains, which finally transform into stable hcp-TiB_2. Due to this precipitation process, the film hardness is ~ 43 GPa for $T_a \leq 900$ °C, although decreasing supersaturation and growth-defect density should result in decreasing hardness, as it is the case for binary TiN layers. When the TiB_2 precipitates grow at constant volume fraction ($T_a \geq 1000$ °C), the decreasing number of particles, the decreasing dislocation – precipitate interaction and, finally, the occurring recrystallization cause a decrease of the Ti(B)N film hardness. A corresponding annealing-strengthening effect is obtained for $Ti_{0.33}Al_{0.67}N$ films, where the metallic part (Ti) of a TiN phase is replaced by Al. During the early stages of the phase-separation, coherent cubic AlN-rich domains are formed causing the hardness to increase, although growth-defect and solid-solution hardening decrease. Further annealing results in a coarsening of these domains to form separate fcc-AlN phases, and hence the dislocation – precipitate elastic interaction diminishes. The concomitant hardness decrease is retarded by the formation of TiN-rich domains. But during further annealing, the precipitates coarsen and recrystallization effects occur, and hence the hardness decreases.

The results obtained show that properties of hard thin films can be designed by their nanostructure and especially by the interfaces separating the nanocrystals. Thus, such films have a high potential to achieve superior properties which can even improve during high-temperature applications, due to diffusion-driven nanostructural rearrangements. Furthermore, the constitution of interfaces in nanocrystalline materials is of vital importance. The results presented for films with supersaturated phases have large implications for the exploration of wear-resistant films and electronic group-III nitride thin films for band gap engineering, as several pseudo-binary nitride or carbide systems exhibit large miscibility gaps. They can be synthesized in quenched metastable solid-solution states by vapor deposition processes operating at kinetically limited conditions. For all investigated films, the nanostructure and hence the interfaces, either generated during growth or post-annealing, are responsible for high or extremely high film-hardness even after annealing at ~ 1000 °C.

We acknowledge the use of the Center for Microanalysis of Materials, University of Illinois, which is partially supported by the U.S. Department of Energy. We are also very grateful to A. Hörling and Profs. J. E. Greene, L. Hultman and I. Petrov for the excellent cooperation.

References

[1] W. Herr, B. Matthes, E. Broszeit, K.H. Kloos: Mater. Sci. Engin. A 140 (1991) 626.
[2] W. Gissler: Surf. Coat. Technol. 68 – 69 (1994) 556.
[3] M. Stoiber, C. Mitterer, T. Schöberl, E. Badisch, G. Fontalvo, R. Kullmer: J. Vac. Sci. Technol. B 21 (3) (2003) 1084.
[4] B. Rother, H. Kappl: Surf. Coat. Technol. 96 (1997) 163.
[5] T.P. Mollart, M. Baker, J. Haupt, A. Steiner, P. Hammer, W. Gissler: Surf. Coat. Technol. 74 – 75 (1995) 491.
[6] P. Losbichler, C. Mitterer: Surf. Coat. Technol. 97 (1997) 567.
[7] W. Gissler, M.A. Baker, J. Haupt, P.N. Gibson, R. Gilmore, T.P. Mollart: Diamond Films Technol. 7 (3) (1997) 165.
[8] J. Ye, S. Ulrich, K. Sell, H. Leiste, M. Stüber, H. Holleck: Surf. Coat. Technol. 174 – 175 (2003) 959.
[9] P. Karvánková, M.G.J. Vepřek-Heijman, M.F. Zawrah, S. Vepřek: Thin Solid Films 467 (2004) 133.
[10] C. Mitterer: J. Sol. State Chem. 133 (1997) 279.
[11] C. Mitterer, M. Rauter, P. Rödhammer: Surf. Coat. Technol. 41 (1990) 351.
[12] P.H. Mayrhofer, C. Mitterer: Surf. Coat. Technol. 133 – 134 (2000) 131.
[13] R. Wiedemann, V. Weihnacht, H. Oettel: Surf. Coat. Technol. 116 – 119 (1999) 302.
[14] R. Wiedemann, H. Oettel, M. Jerenz: Surf. Coat. Technol. 97 (1997) 313.
[15] R. Wiedemann, H. Oettel: Surf. Engin. 14 (1998) 299.
[16] P.H. Mayrhofer, H. Willmann, C. Mitterer: Thin Solid Films 440 (2003) 174.
[17] P.H. Mayrhofer, A. Hörling, L. Karlsson, J. Sjölén, T. Larsson, C. Mitterer, L. Hultman: Appl. Phys. Lett. 83(10) (2003) 2049.
[18] S. Vepřek, S. Reiprich: Thin Solid Films 268 (1995) 64.

[19] S. Vepřek, P. Nesládek, A. Niederhofer, F. Glatz: NanoStruct. Mat. 10 (5) (1998) 679.
[20] A. Niederhofer, T. Bolom, P. Nesládek, K. Moto, C. Eggs, D.S. Patil, S. Vepřek: Surf. Coat. Technol. 146–147 (2001) 183.
[21] S. Vepřek, P. Nesládek, A. Niederhofer, F. Glatz, M. Jílek, M. Šíma: Surf. Coat. Technol. 108–109 (1998) 138.
[22] S. Vepřek, A.S. Argon: Surf. Coat. Technol. 146–147 (2001) 175.
[23] S. Vepřek: J. Vac. Sci. Technol. A 17(5) (1999) 2401.
[24] J. Patscheider, T. Zehnder, M. Diserens: Surf. Coat. Technol. 146–147 (2001) 201.
[25] F. Kunc, J. Musil, P.H. Mayrhofer, C. Mitterer: Surf. Coat. Technol. 174–175 (2003) 744.
[26] W.-D. Münz: J. Vac. Sci. Technol. A 4 (6) (1986) 2717.
[27] S. PalDey, S.C. Deevi: Mat. Sci. Engin. A 342 (1–2) (2002) 58.
[28] T. Suzuki, Y. Makino, M. Samandi, S. Miyake: J. Mater. Sci. 35 (2000) 4193.
[29] F. Adibi, I. Petrov, L. Hultman, U. Wahlström, T. Shimizu, D. McIntyre, J.E. Greene, J.-E. Sundgren: J. Appl. Phys. 69 (9) (1991) 6437.
[30] R. Prange, R. Cremer, D. Neuschütz: Surf. Coat. Technol. 133–134 (2000) 208.
[31] P. Panjan, B. Navinšek, M. Čekada, A. Zalar: Vacuum 53 (1999) 127.
[32] O. Knotek, A. Barimani: Thin Solid Films 174 (1989) 51.
[33] R.A. Andrievskii, A. Anisimova, V.P. Anisimov: Thin Solid Films 205 (1991) 171.
[34] P. Holubar, M. Jílek, M. Šíma: Surf. Coat. Technol. 133–134 (2000) 145.
[35] P.H. Mayrhofer, G. Tischler, C. Mitterer: Surf. Coat. Technol. 142–144 (2001) 78.
[36] P.H. Mayrhofer, F. Kunc, J. Musil, C. Mitterer: Thin Solid Films 415 (2002) 151.
[37] A. Hörling, L. Hultman, M. Odén, J. Sjölen, L. Karlsson: J. Vac. Sci. Technol. A 20 (5) (2002) 1815.
[38] L. Hultman: Vacuum 57 (2000) 1.
[39] C. Suryanarayana: Int. Mat. Rev. 40(2) (1995) 41.
[40] A. Grill: Diam. Relat. Mater. 8 (1999) 428.
[41] C. Faure, W. Hänni, C.J. Schmutz, M. Gervanoni: Diam. Relat. Mater. 8 (1999) 830.
[42] P.B. Mirkarimi, K.F. McCarty, D.L. Medlin: Mater. Sci. Engin. Reports 21 (1997) 47.
[43] J.M. Schneider, W.D. Sproul, A. Matthews: Surf. Coat. Technol. 98 (1998) 1473.
[44] W. Schintlmeister, W. Wallgram, J. Kanz, K. Gigl: Wear 100 (1984) 153.
[45] H. Holleck, V. Schier: Surf. Coat. Technol. 76–77 (1995) 328.
[46] C. Mitterer, P. Losbichler, F. Hofer, P. Warbichler, P.N. Gibson, W. Gissler: Vacuum 50(3–4) (1998) 313.
[47] P. Losbichler, C. Mitterer, P.N. Gibson, W. Gissler, F. Hofer, P. Warbichler: Surf. Coat. Technol. 94–95 (1997) 297.
[48] A.A. Voevodin, J.P. O'Neill, J.S. Zabinski: Surf. Coat. Technol. 116–119 (1999) 36.
[49] R. Gilmore, M.A. Baker, P.N. Gibson, W. Gissler, M. Stoiber, P. Losbichler, C. Mitterer: Surf. Coat. Technol. 108–109 (1998) 345.
[50] H. Holleck, H. Schulz: Surf. Coat. Technol. 36 (1988) 707.
[51] H. Holleck, M. Lahres: Mat. Sci. Engin. A 140 (1991) 609.
[52] Y. Quiaoquin, Z. Lihua, W. Lijun, D. Haiquing, W. Lishi: J. Mater. Sci. Lett. 15 (1996) 11.
[53] M. Stüber, V. Schier, H. Holleck: Surf. Coat. Technol. 74/75 (1995) 833.
[54] C.S. Pande, R.A. Masumura, R.W. Armstrong: NanoStruct. Mat. 2 (1993) 323.
[55] J.E. Carsley, J. Ning, W.W. Milligan, S.A. Hackney, E.C. Aifantis: NanoStruct. Mat. 5(4) (1995) 441.
[56] H. Hahn, K.A. Padmanabhan: NanoStruct. Mat. 6 (1995) 191.
[57] A.E. Romanov: NanoStruct. Mat. 6 (1995) 125.
[58] C. Moelle, H.J. Fecht: NanoStruct. Mat. 3 (1993) 93.
[59] E. Arzt: Acta Mater. 46 (1998) 5611.
[60] E.O. Hall: Proc. Phys. Soc. B 64 (1951) 747.
[61] N.J. Petch: J. Iron Steel Inst. 174 (1953) 25.
[62] A.E. Romanov: NanoStruct. Mater. 6 (1995) 125.
[63] D. Tabor: The Hardness of Metals, Clarendon Press, Oxford, (1951).
[64] R.W. Cahn, P. Haasen (Eds.): Physical Metallurgy, North-Holland, New-York, (1996).
[65] D.M. Marsh: Proc. R. Soc. A 279 (1964) 420.
[66] A. Kelly, N.H. MacMillan: Strong Solids, Clarendon Press, Oxford (1986).
[67] J. Schiøtz, F.D. Di Tolla, K.W. Jacobsen: Nature 391 (1998) 561.
[68] J. Musil, J. Vlček: Mater. Chem. Phys. 54 (1998) 116.
[69] C. Suryanarayana, D. Mukhopadhyay, S.N. Patankar, F.H. Froes: J. Mater. Res. 7 (1992) 2114.
[70] H. Gleiter: NanoStruct. Mater. 1 (1992) 1.
[71] R.W. Siegel, G.E. Fougere: NanoStruct. Mater. 6 (1995) 205.
[72] I. Petrov, L. Hultman, J.-E. Sundgren, J.E. Greene: J. Vac. Sci. Technol. A 10(2) (1992) 265.
[73] F.J. Humphreys, M. Hatherly: Recrystallization and Related Annealing Phenomena, Elsevier, Oxford, (1995).
[74] J.K. Gimzewski, A. Humbert: IBM J. Res. Develop. 30(5) (1986) 472.
[75] R.F. Bunshah: Handbook of Deposition Technologies for Films and Coatings, Noyes Publications, New Jersey, (1994).
[76] H. Holleck: Surf. Coat. Technol. 36 (1988) 151.
[77] L. Hultman: Key Engin. Mat. 103 (1995) 181.
[78] P.H. Mayrhofer, C. Mitterer, J.G. Wen, J.E. Greene, I. Petrov: Appl. Phys. Lett. (2005) in press.
[79] P.H. Mayrhofer, C. Mitterer, J.G. Wen, I. Petrov, J.E. Greene: Acta Mater. to be submitted (2005).
[80] P.H. Mayrhofer, M. Stoiber, C. Mitterer: Scripta Mater. (2005) accepted.
[81] I. Petrov, V. Orlinov, I. Ivanov, J. Kourtev: Contrib. Plasma Phys. 28 (1988) 2.
[82] M. Berger, L. Karlsson, M. Larsson, S. Hogmark: Thin Solid Films 401 (2001) 179.
[83] T.B. Massalsky: Binary Alloy Phase Diagrams; American Society for Metals, Metals Park, (1986).
[84] V. Ferrando, D. Marre, P. Manfrinetti, I. Pallecchi, C. Tarantini, C. Ferdeghini: Thin Solid Films 444 (2003) 91.
[85] P. Vajeeston, P. Ravindran, C. Ravi, R. Asokamani: Phys. Rev. B 63 (2001) 045115.
[86] R.G. Munro: J. Res. Natl. Inst. Stand. Technol. 105 (2000) 709.
[87] H. Holleck: J. Vac. Sci. Technol. A 4 (6) (1986) 2661.
[88] J. Musil: Surf. Coat. Technol. 125 (2000) 322.
[89] E.J. Mittemeijer, P. Scardi: Diffraction Analysis of the Microstructure of Materials, Springer, Berlin (2004).
[90] H. Oettel, R. Wiedemann: Surf. Coat. Technol. 76–77 (1995) 265.
[91] A.W. Weimer: Carbide, Nitride and Boride Materials Synthesis and Processing, New York, Chapman and Hall, 1997.
[92] E.M. Schulson, T.P. Weihs, P.V. Veins, I. Baker: Acta Metall. 33 (1985) 1585.
[93] P. Karvánková, M.G.J. Vepřek-Heijman, O. Zindulky, A. Bergmaier, S. Vepřek: Surf. Coat. Technol. 163–164 (2003) 149.
[94] Powder Diffraction File (Card 33–397 for steel substrate, Card 35–1375 for Ni-Cr-Fe phase), JCPDS-International Center for Diffraction Data, Swarthmore, PA, 2001.
[95] P.H. Mayrhofer, C. Mitterer: Mater. Res. Soc. Proc. Boston, MA, 2004, in press.
[96] J. Schiøtz, T. Vegge, F.D. Di Tolla, K.W. Jacobsen: Phys. Rev. B 60(17) (1999) 11971.
[97] L. Karlsson, H. Norden, H. Odelius: Acta Metall. 36 (1) (1988) 1.
[98] D.A. Porter, K.E. Easterling: Phase Transformations in Metals and Alloys, Stanley Thornes, Cornwall, (2000).
[99] J.W. Cahn: Acta Met. 9 (1961) 795.
[100] H.-D. Männling, D.S. Patil, K. Moto, M. Jílek, S. Vepřek: Surf. Coat. Technol. 146–147 (2001) 263.
[101] A. Niederhofer, P. Nesládek, H.-D. Männling, K. Moto, S. Vepřek, M. Jílek: Surf. Coat. Technol. 120–121 (1999) 173.
[102] S. Vepřek, A.S. Argon: J. Vac. Sci. Technol. B 20(2) (2002) 650.
[103] G. Kresse, J. Furthmüller: Phys. Rev. B 54 (1996) 11169; Computat. Mat. Sci. 6 (1996) 15.
[104] P. Raybaud, J. Hafner, G. Kresse, H. Toulhoat: Phys. Rev. Lett. 80 (1998) 1481.
[105] G. Pezzotti, K. Ota, H.-J. Kleebe: J. Am. Ceram. Soc. 79 (9) (1996) 2237.
[106] E. Badisch, C. Mitterer, P.H. Mayrhofer, G. Mori, R. Bakker, H. Störi: Thin Solid Films 2004;460:125.
[107] Q. Xia, H. Xia, A. Ruoff: J. Appl. Phys. 73 (1993) 8198.
[108] H.L. Skriver: LMTO Method: Muffin-Tin Orbital and Electronic Structures; Springer Series in Solid State Sciences: 41, Springer, Berlin, (1984).

[109] H.W. Hugosson, H. Högberg, M. Algren, M. Rodmar, T.I. Selinder: J. Appl. Phys. 93 (8) (2003) 4505.
[110] M. Berger, M. Larsson, S. Hogmark: Surf. Coat. Technol. 124 (2000) 253.
[111] J.G. Ryan, S. Roberts, G.J. Slusser, E.D. Adams: Thin Solid Films 153 (1987) 329.
[112] J.-K. Lee: J. Cryst. Growth 246 (2002) 113.
[113] R. Gilmore, M.A. Baker, P.N. Gibson, W. Gissler: Surf. Coat. Technol. 116–119 (1999) 1127.
[114] C. Pfohl, A. Bulak, K.-T. Rie: Surf. Coat. Technol. 131 (2000) 141.
[115] R. Lohmann, E. Österschulze, K. Thoma, H. Gärtner, W. Herr, B. Matthes, E. Broszeit, K.-H. Kloos: Mater. Sci. Engin. A 139 (1991) 259.
[116] M.S. Wong, J.C. Lee: Surf. Coat. Technol. 120–121 (1999) 194.
[117] I. Petrov, P.B. Barna, L. Hultman, J.E. Greene: J. Vac. Sci. Technol. A 21(5) (2003) 117.
[118] P.B. Barna, M. Adamik: Thin Solid Films 317 (1998) 27.
[119] S. Yip: Nature 391 (1998) 532.
[120] M.E. Eberhart, D.D. Vvedensky: Phys. Rev. Lett. 85 (1987) 61.
[121] E.P. George, C.L. White, J.A. Horton: Scripta Metall. Mater. 25 (1991) 1259.

(Received November 29, 2004; accepted February 15, 2005)

Correspondence address

Dr. P. H. Mayrhofer
Department of Physical Metallurgy and Materials Testing
University of Leoben
Franz Josef Straße 18, A-8700 Leoben, Austria
Tel.: +43 3842 402 4211
Fax: +43 3842 402 4202
E-mail: mayrhof@unileoben.ac.at